metals

MDPI

Article

Numerical Model for Predicting Bead Geometry and Microstructure in Laser Beam Welding of Inconel 718 Sheets

Iñigo Hernando *, Jon Iñaki Arrizubieta, Aitzol Lamikiz and Eneko Ukar

Department of Mechanical Engineering, Faculty of Engineering Bilbao, University of the Basque Country (UPV/EHU), Plaza Torres Quevedo 1, 48013 Bilbao, Spain; joninaki.arrizubieta@ehu.eus (J.I.A.); aitzol.lamikiz@ehu.eus (A.L.); eneko.ukar@ehu.eus (E.U.)

* Correspondence: inigo.hernando@ehu.eus; Tel.: +34-946-017-347

Received: 19 June 2018; Accepted: 4 July 2018; Published: 12 July 2018

Abstract: A numerical model was developed for predicting the bead geometry and microstructure in laser beam welding of 2 mm thickness Inconel 718 sheets. The experiments were carried out with a 1 kW maximum power fiber laser coupled with a galvanometric scanner. Wobble strategy was employed for sweeping 1 mm wide circular areas for creating the weld seams, and a specific tooling was manufactured for supplying protective argon gas during the welding process. The numerical model takes into account both the laser beam absorption and the melt-pool fluid movement along the bead section, resulting in a weld geometry that depends on the process input parameters, such as feed rate and laser power. The microstructure of the beads was also estimated based on the cooling rate of the material. Features such as bead upper and bottom final shapes, weld penetration, and dendritic arm spacing, were numerically and experimentally analyzed and discussed. The results given by the numerical analysis agree with the tests, making the model a robust predictive tool.

Keywords: laser; welding; LBW; model; microstructure; SDAS; bead seam; wobble strategy; Inconel 718

1. Introduction

Laser beam welding (LBW) is a material-joining technique that applies laser radiation to melt the base material and create the welding joint. LBW process is related to other traditional welding methods, such as electron beam welding (EBW), tungsten plasma arc welding (PAW), or inert gas tungsten arc welding (TIG). LBW applies a high power industrial laser to create a narrow and deep melt pool between the parts to be welded. Laser is a highly concentrated heat source that can be easily automated and installed on industrial welding cells, providing high welding speeds for many industrial applications. Nevertheless, factors such as the laser beam quality or the processed materials have a great influence on the resulting geometry, microstructure, and residual stress distribution. Therefore, final results are directly dependent on the process input parameters [1], which means that process parameters must be carefully selected for achieving the desired quality [2].

LBW modeling represents a basic tool for predicting the temperature field and giving accurate information about shape of the melt pool and final shape of the bead, depending on the process parameters (welding speed, laser power, workpiece geometry, etc.) [3–5]. This fact has a direct impact on reducing the costs derived from experimental tests [6].

Modern aircraft engines require materials capable of withstanding high temperatures without lowering their mechanical properties. In order to fulfil this task, nickel-based alloys comprise about 50% of the total weight of the engines used in aerospace industry, providing high temperature strength and good resistance against wear or corrosion, thanks to their chemical stability [7]. Aeronautical

structures design and fabrication searches for minimum weight models that may put up with several flight work conditions. Since Ni alloys' machinability is relatively low, and the cost of the material is high, welding techniques present high advantages over machining. On the one hand, welding can be used for building complex structures from smaller parts and, on the other hand, wasted material and chip formation is drastically reduced.

Inconel 718 superalloy is widely used in gas turbine components, such as tail bearing housings (TBH), which have to deal with high temperature gradients and corrosive environments. The strength of the material comes mainly from small γ' and γ'' precipitates that are high in Ni content [8]. On the other hand, despite that the Inconel 718 alloy has a reasonably good resistance against weld solidification cracking, it is slightly prone to the appearance of microfissures in the heat affected zone (HAZ) [9], so LBW is an appropriate joining method, as it affects just a narrow zone.

Regarding this fact, modeling and study are needed in order to check weld integrity, as LBW is an innovative assembling method both for dispensing rivets and for its good qualities compared to other conventional welding techniques [10]. LBW is also suitable for joining both similar and dissimilar metal alloys. This last case is given the possibility to benefit from the properties that each welded part can offer for different working conditions [11], giving an increasing value to the dissimilar metal alloys' welding process in the aerospace industry, due to its direct impact on cost reduction and design flexibility [12].

Furthermore, LBW has arisen as an alternative to electron beam welding (EBW), which can only be used in a vacuum chamber, and requires a more complex fixturing, which results in a much more expensive process.

In terms of pores formation, nickel-based alloys with chromium (as Inconel 718) are susceptible to this phenomenon during the welding process, having to resort to protective gases in order to avoid pores [13].

The laser power level that materials absorb can be reasonably predicted, so the effects of the heat input may be accurately estimated by a numerical model [14]. The absorptivity of the material represents the ratio of the energy that the workpiece absorbs, it is one of the bases for any heat transfer calculation [15], and hence, modeling must consider this characteristic for any reliable result. Moreover, other effects need to be considered in laser welding processes, such as convective and thermocapillary forces that cause deformations during solidification after the melting phase. These forces are generated due to a decrease of the surface tension of the molten material as temperature increases, which leads to material flow between hot and cold regions [16]. This phenomenon, named as the Marangoni effect, has a direct impact on the weld bead geometry [17]. Therefore, the model must consider this effect in order to achieve the desired accuracy and predict the welding profile.

At the beginning of the LBW technology, Swift-Hook and Gick stated that lasers opened a wide range of possibilities according to deep welds [18], and Klemens declared that many factors, such as heat, vapor flow, gravity, or surface tension, are directly connected with the final shape of the seam. Moreover, the need for experimental tests for validating the theoretical heat models took force for identifying unknown factors [19].

In the 1980s, Mazumder praised the importance of better understanding the melt pool generation and fluid flow, in order to improve the potential of the mathematical models, making them predictive powerful tools [15]. In the same way, Goldak et al. asserted that the prediction of aspects such as the strength of the welded structures, which is directly related to residual stress or distortions, called for precise analysis of the thermal cycles for further modeling [20].

Afterwards, Bonollo et al. assured that the laser welding dynamics were not entirely understood, despite that theoretical evaluation and subsequent experimental validation had enabled development of the comprehension of the LBW technique [21]. This statement was confirmed by Kaplan et al., who placed value on modeling for improving the physical understanding of the LBW process [22]. Ducharme et al., for their part, pointed out that modeling allowed for demonstration of the relationship between the keyhole and the melt pool [23].

Sudnik et al. alleged the need for new theoretical work, in order to better the laser welding process, as well as its control and the description of the defects. This was grounded on the fact that many heat conduction models did not achieve the desired accuracy when predicting the weld bead geometry [24]. Nevertheless, Tsirkas et al. pointed the difficulty of modeling the welding process, as thermal, mechanical, and metallurgical phenomena take place at the same time [25]. Furthermore, Gery et al. concluded that the experimental work is mandatory for determining relations between heat source models and subsequent empirical testing [26].

Later, Kazemi and Goldak continued maintaining the idea that modeling the laser keyhole welding was still challenging, and defended the idea of simplifying the models for describing the temperature fields [6]. In turn, Zhao et al. affirmed that the coexistence of three different phases (plasma, liquid, and solid) added to the complex keyhole behavior and the forces acting in the weld pool made modeling still difficult [27].

Likewise, Kubiak et al. underlined the necessity of an innovative focusing on the theory and numerical solution techniques used for LBW, as this process offers characteristic heat distributions compared to traditional welding methods [28]. However, Zhang et al. pointed out that despite the advances in laser deep penetration knowledge due to numerical simulation, many issues still remain unexplored [29].

For this reason, it is concluded that there is a need, in the aerospace industry, to develop a model that predicts the geometry of the resulting joint when welding thin Inconel 718 plates. Therefore, a model that considers the melt pool dynamics during the welding process is developed. The model takes into account gravity, Marangoni, and surface forces caused by the curvature developed by the weld bead. Moreover, the numeric tool is capable of predicting the generated secondary dendrite arm spacing based on the thermal field variations during the process. In addition, the obtained results are experimentally validated under different conditions. Employed nomenclature is detailed in Table 1.

Table 1. Employed symbols and nomenclature.

Symbol	Description	Unit
u	Fluid velocity in the X axis direction.	$m{\cdot}s^{-1}$
v	Fluid velocity in the Y axis direction.	$m{\cdot}s^{-1}$
U	Absolute fluid velocity.	$m{\cdot}s^{-1}$
Δx	Element size in the X axis direction.	m
Δy	Element size in the Y axis direction.	m
ρ	Material density.	$kg{\cdot}m^{-3}$
p	Pressure value.	$N{\cdot}m^{-2}$
μ	Material viscosity.	$kg{\cdot}m^{-1}{\cdot}s^{-1}$
$\underline{g}$	Gravitational acceleration constant.	$m{\cdot}s^{-2}$
$\overrightarrow{e}$	$Y+$ direction unitary vector.	-
γ	Volume fraction (solid/liquid).	-
f_l	Liquid fraction	-
f_s	Surface forces.	N
σ	Surface tension.	$N{\cdot}m^{-1}$
$\frac{d\sigma}{dT}$	Surface tension variation regarding the temperature.	$N{\cdot}m^{-1}{\cdot}K^{-1}$
κ	Surface curvature.	m^{-1}
$\overrightarrow{n}$	Vector normal to the surface (solid/liquid–gas interface).	-
β	Coefficient of liquid thermal expansion.	K^{-1}
c	Specific energy.	$J{\cdot}kg^{-1}{\cdot}c$
k	Heat conductivity.	$W{\cdot}m^{-1}{\cdot}K^{-1}$
S_L	Fusion latent heat.	$J{\cdot}kg^{-1}$

Table 1. *Cont.*

Symbol	Description	Unit
T	Temperature.	K
T_S	Solidus temperature.	K
T_L	Liquidus temperature.	K
T_∞	Room temperature.	K
t	Time variable.	S
Δt	Time step.	S
P	Laser power.	W
q_{laser}	Laser beam intensity.	$W{\cdot}m^{-2}$
q_{losses}	Energy losses due to radiation and convection.	$W{\cdot}m^{-2}$
r_{out}	Outer radius of the laser beam in the wobble strategy.	M
r_{in}	Inner radius of the laser beam in the wobble strategy.	M
α	Absorptivity.	-
h	Convection coefficient.	$W{\cdot}m^{-2}\,K^{-1}$
ε	Emissivity.	-
σ_b	Stefan–Boltzmann coefficient.	$W{\cdot}m^{-2}\,K^{-4}$
δ	Angle between the laser beam and the normal vector to the surface	rad
v_f	Welding feed rate	$Mm{\cdot}s^{-1}$
v_p	Peripheral speed in the wobble operation	$mm{\cdot}s^{-1}$

2. Developed Model

2.1. Model Basis

The proposed model is based on solving the continuity (1), momentum (2), and energy conservation (3) equations, in order to obtain the pressure, velocity, and temperature fields of each element, respectively. The coupled pressure-velocity equations are solved using the SIMPLE algorithm proposed by Patankar [30] and a fully implicit scheme is used.

$$\frac{\partial \rho}{\partial t} + \frac{\partial}{\partial x}(\rho{\cdot}u) + \frac{\partial}{\partial y}(\rho{\cdot}v) \;=\; 0 \tag{1}$$

$$\frac{\partial}{\partial t}(\rho{\cdot}\phi) + \frac{\partial}{\partial x}(\rho{\cdot}u{\cdot}\phi) + \frac{\partial}{\partial y}(\rho{\cdot}v{\cdot}\phi) \;=\; -\frac{\partial p}{\partial x} + \frac{\partial}{\partial x}\left(\mu{\cdot}\frac{\partial \phi}{\partial x}\right) - \frac{\partial p}{\partial y} + \frac{\partial}{\partial y}\left(\mu{\cdot}\frac{\partial \phi}{\partial y}\right) + S_m \tag{2}$$

$$\frac{\partial}{\partial t}(\rho{\cdot}c{\cdot}T) + \frac{\partial}{\partial x}(\rho{\cdot}c{\cdot}u{\cdot}T) + \frac{\partial}{\partial y}(\rho{\cdot}c{\cdot}v{\cdot}T) \;=\; \frac{\partial}{\partial x}\left(k{\cdot}\frac{\partial T}{\partial x}\right) + \frac{\partial}{\partial y}\left(k{\cdot}\frac{\partial T}{\partial y}\right) + S_e \tag{3}$$

The momentum generation term (S_m) includes the buoyancy force (S_b), generated as a consequence of the density difference, and the velocity reduction term (S_d), introduced in those elements where the material is in solid state. Material is considered completely rigid and incompressible when it is in solid state, therefore, the velocity of the material in the solid region is zero. This is modeled by the second term in Equation (4), where the parameter f_l, which represents the liquid fraction, has a zero value in the solid and a unit value in the liquid. In order to avoid numerical instabilities due to a zero in the denominator at the solid region, the coefficient e_0 must have a small value (10^{-3} in the present model). Moreover, the coefficient C must have a high value in order to make zero the velocity of the fluid flow in the solid region $C = 10^6$ $kg{\cdot}m^{-3}{\cdot}s^{-1}$ [31].

$$S_m \;=\; S_b + S_d \;=\; \rho{\cdot}g{\cdot}\beta{\cdot}(T - T_\infty).\vec{e} - \frac{C{\cdot}(1 - f_l)}{f_l^3 + e_0}{\cdot}U \tag{4}$$

Regarding the energy generation term (S_e), Equation (5) includes the latent heat (S_L) and the heat exchange at the substrate surface (S_C). Inside this second term, the energy radiated by the laser beam (q_{laser}) and the heat losses due to radiation and convection (q_{losses}) are included. As no

material vaporization is expected, the model includes only the fusion latent heat, which is defined in Equation (6).

$$S_e = S_L + S_C = S_L + q_{laser} - q_{losses} \quad (5)$$

$$S_L = \rho \cdot \frac{\partial L}{\partial t} = \rho \cdot \frac{\partial L}{\partial T} \cdot \frac{\partial T}{\partial t} \quad (6)$$

The energy input at the surface can be approximated as a ring-type source, generated by a fast-moving laser spot that follows a wobble strategy, as is shown in Figure 1. Therefore, the energy input in a surface element located at an x and y planar distance from the laser beam center point is defined by means of Equation (7). As the free surface can deform freely, the absorptivity value (α) is modified as a function of the angle between the laser beam centerline and the normal vector to the free surface (δ). On the other hand, radiation and convection losses at the surface of the substrate are described by Equation (8), where n is the number of free-faces of a certain element located on the surface.

$$q_{laser} = \frac{2 \cdot \alpha \cdot cos(\delta) \cdot P}{\pi \cdot (r_{out}^2 - r_{in}^2)} \quad (7)$$

$$q_{losses} = n \cdot \left[h \cdot (T - T_\infty) + \varepsilon \cdot \sigma_b \cdot \left(T^4 - T_\infty^4 \right) \right] \quad (8)$$

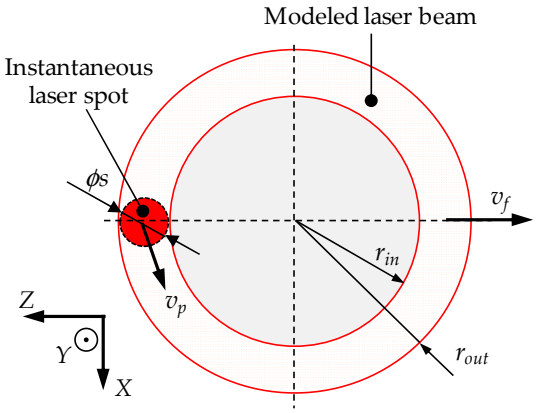

Figure 1. Instantaneous laser spot and modeled laser beam in wobble strategy.

The model considers conduction and diffusion as heat transfer mechanisms within the material. Moreover, the volume of fluid (VOF) Equation, (9), is solved to determine the material movement and the variation of the free surface. For tracking the interface, the interface capturing method is used because, unlike other methods, it does not introduce restrictions to the evolution of the free surface. This method gives the position of the boundary between the different phases by using a scalar transport variable. The volume fraction (γ) becomes a zero value in the gas and a unit value in the base material (solid or liquid). Therefore, the interface is defined as the transition zone where γ takes a value between zero and the unit.

$$\frac{\partial \gamma}{\partial t} + \nabla(\gamma \cdot U) = 0 \quad (9)$$

The residue value to ensure the convergence of the results is set to a 10^{-3} value between two subsequent iterations. The same criteria are used for mass, momentum, energy conservation, and VOF equations.

2.2. Initial and Boundary Conditions

In order to start the simulation, the initial temperature of all elements must be defined. Since no preheating stage has been considered, all nodes are supposed to be at room temperature (T_∞ = 298 K).

Therefore, the whole substrate is in solid state at the initial stage, and all the elements have a zero-velocity value.

Velocity, pressure, and temperature values are determined at the limits of the model by means of the boundary conditions, see Figure 2. On the one hand, a zero-pressure gradient condition is established in all the boundaries. On the other hand, a zero-velocity vector variation condition is established in all boundary faces. Lastly, in terms of temperature boundaries, the nodes next to the control volume are forced to be at room temperature (T_∞ = 298 K). This is equivalent to consider a first specie or Dirichlet boundary condition, Equation (10).

$$q = k \cdot \left(\frac{\partial T}{\partial x} + \frac{\partial T}{\partial y} \right) \tag{10}$$

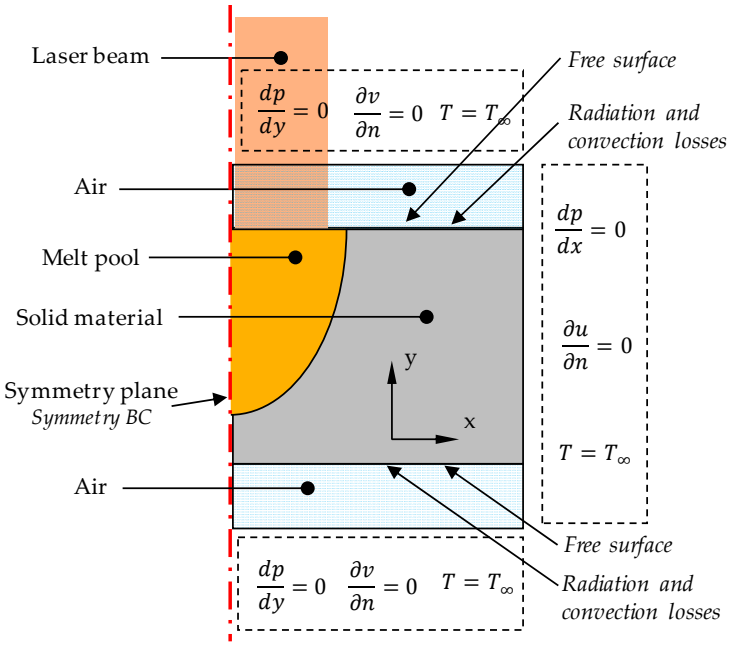

Figure 2. Applied boundary conditions for modeling the welding process.

With the aim of reducing unnecessary computational cost and based on the symmetric nature of the modeled problem, just half of the volume is simulated. The following boundary conditions are set in the symmetry plane:

$$\frac{dT}{dy} = 0; \; u = 0; \; \frac{dv}{dx} = 0 \tag{11}$$

2.3. Surface Forces

Movement of the molten material is generated due to surface forces, see Equation (12). On the one hand, a force normal to the surface takes place due to the curvature developed by the interface between the air and substrate. On the other hand, Marangoni forces are generated because of the surface stress variation regarding the temperature variation. In addition, buoyancy forces are included in the model, which generate a downwards force. All forces considered in the model are shown in Figure 3.

$$f_S = \left[\sigma \cdot \kappa \cdot \vec{n} + \frac{d\sigma}{dT} \left[\nabla T - \vec{n} \cdot \left(\vec{n} \cdot \nabla T \right) \right] \right] \tag{12}$$

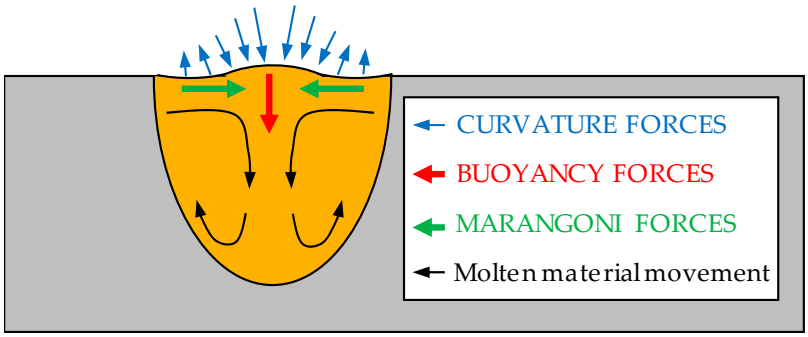

Figure 3. Material movement due to the surface and buoyancy forces.

2.4. Microstructure

The internal structure of material after melting and solidifying depends directly on the process cooling rate. When the temperature drops below the liquidus temperature (T_L), columnar dendritic microstructure is formed until the solidus temperature (T_S) is reached. This temperature phase-change range is named as the mushy zone [32].

The interplanar spacing between different dendrites can be estimated based on the cooling rate and the boundary temperatures where the material undergoes the phase changes, which are the T_L and the γ/laves eutectic temperature (T_e). At this juncture, dendritic columns grow mainly in the energetically favorable crystallographic directions, forming the principal axis and, to a lesser extent, in the other transverse secondary directions [9]. The secondary dendrite arm spacing (SDAS) is measured in this research test for subsequent thermal model validation by means of Equation (13). To this end, the mean values are calculated based on ten different measurements for each analyzed welding bead. SDAS is measured in µm, and C is a constant that depends on the material. For the specific case of the Inconel 718, this constant takes a value of 10 [33].

$$SDAS = C \cdot \left(\frac{T_L - T_e}{\frac{dT}{dt}} \right)^{\frac{1}{3}} \quad (13)$$

The Inconel 718 is a widely used and studied material, and therefore, many authors have contributed with their research to the determination of these reaction temperatures. In the present investigation, the values given by Eiselstein for the cooling case are considered [34]: 1260 °C and 1177 °C for the liquidus temperature (T_L) and the γ/laves eutectic temperature (T_e), respectively (Table 2).

Table 2. Inconel 718 cooling temperatures.

Reaction Stage	Value (°C)
Liquidus on cooling	1260
Solidus on cooling	1227
γ/laves eutectic on cooling	1177

3. Proposed Methodology for the Model Validation

Validation has been carried out using FL010 1kW fiber laser from Rofin FL010 (ROFIN-SINAR Laser, Hamburg, Germany) with an output fiber of 100 µm coupled to galvanometric scan head hurrySCAN® 25 from SCANLAB (SCANLAB GmbH, Munich, Germany) with a focus length of 265 mm, maximum workspace of 120 × 120 mm^2, and maximum feed rate of 10,000 mm·s^{-1}. Scan head allows fast movements of the laser beam because of the low inertia of the moving mirrors, giving, as a result, high velocities and accelerations without losing positioning accuracy. Therefore, the laser beam

motion is fast enough to consider as a ring-type spot of 1 mm diameter that moves at a v_f feed rate speed. In this case, a wobble strategy is used for the welding process, see Figure 4. This method allows one to fill an area by describing rings, so a suitable relation between the feed rate (v_f) and the peripheral speed (v_p) is implemented for achieving minimum overlap and no space among consecutive rings. Therefore, the laser spot must spend the same time for tracing a loop (orbital motion) and for advancing a spot diameter distance (linear movement).

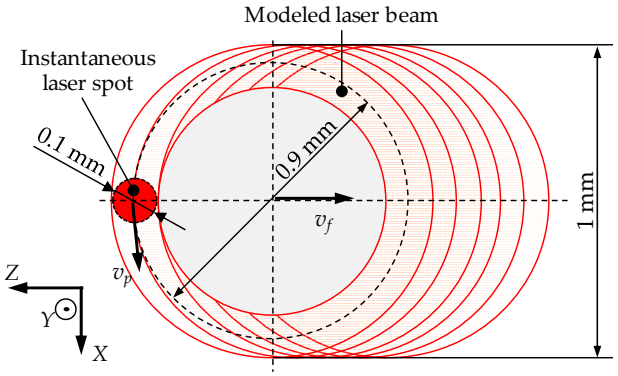

Figure 4. Wobble scanning technique employed for the welding operation.

The selected continuous laser powers for welding the 2 mm thickness Inconel 718 sheets are 350 W, 400 W, 450 W, and 500 W, in combination with two different feed rates: 3 mm·s^{-1} and 5 mm·s^{-1}. The seam length is of 30 mm, enough to ensure steady state is achieved during welding track. All process parameters are detailed in Table 3. Afterwards, all the samples are cut at a 20 mm distance from the beginning of the weld, encapsulated and polished for Marble solution etching, Figure 5. The geometry of the weld beads is revealed by this chemical attack, in order to analyze their cross shape and compare them with the results provided by the model. Moreover, secondary dendrite arm spacing (SDAS) in the samples is measured for the cases where the minimum and maximum powers are applied (350 W and 500 W, respectively). Finally, the measured SDAS is compared with the values predicted by the numerical model.

Table 3. Process parameters for the different tests.

Test Number	Laser Power (W)	Feed Rate (mm·s^{-1})	Peripheral Speed (mm·s^{-1})	Argon Feed (l·min^{-1})	Seam Length (mm)	Wobble Diameter (mm)
1	350	3	84.8	24	30	0.9
2	350	5	141.4	24	30	0.9
3	400	3	84.8	24	30	0.9
4	400	5	141.4	24	30	0.9
5	450	3	84.8	24	30	0.9
6	450	5	141.4	24	30	0.9
7	500	3	84.8	24	30	0.9
8	500	5	141.4	24	30	0.9

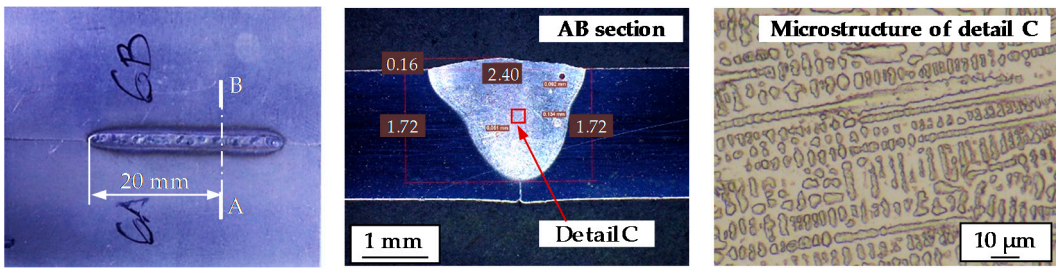

Figure 5. Upper view (**left**), cross section (**center**) and detail of the microstructure (**right**) of the Test 6.

3.1. Model Parameters

The modeled cross section has an 8 × 4 mm size in the X and Y directions, respectively. Notice that in $X = 0$, a symmetry boundary condition is considered (see Figure 2). The distant face in this direction must be placed far enough from the laser beam source in order to avoid any disturbances in the generated thermal field, but without putting it too far away, in order to avoid computational cost having been increased in vain. On the other hand, in the Y direction, a 1 mm layer of air is considered below and above the sheets to be welded, which is enough for allowing the free movement of the air-filled elements.

Defining an appropriate element size is critical when achieving a good relation between accuracy and computational cost. After testing with 0.1, 0.075, 0.05, and 0.025 mm size elements and evaluating the obtained accuracy and the elapsed time required for the simulation, it is considered that a 0.05 mm element size is the optimum value. As can be observed in Figure 6, after simulating Test 4 with different element sizes, an error below 5% is obtained with a 0.05mm element size when the depth of the weld bead is measured, together with an elapsed time of 392.95 s.

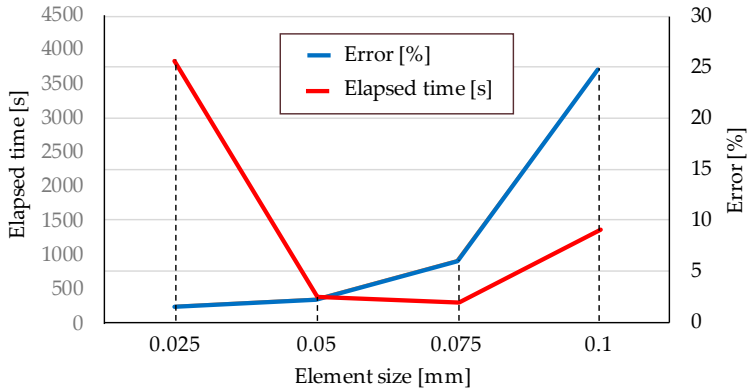

Figure 6. Variation of the elapsed time required for running the simulation and the obtained error compared with the experimentally measured depth of the weld bead as the element size varies for the case of the Test 4.

Besides, the obtained results depend on the time increment used in simulation. For the present validation, a 0.001 s time step is used. A higher time step means that fewer steps are required for sweeping the desired time interval, whereas a smaller time step means the opposite. However, higher time step results in higher variations of the pressure and velocity fields, and consequently, the number of required iterations before achieving the desired accuracy is also increased. In addition, instabilities may appear, resulting in the necessity of lowering the under-relaxation factors used in the SIMPLE algorithm (0.8 and 0.5 for the pressure and velocities calculation, respectively).

The cooling stage has direct influence on the final shape of the melt pool [31], as well as the developed microstructure [35]. Therefore, a cooling period is simulated, whose duration is twice the time required by the laser beam to pass over the modeled cross section. Total process simulation times of 1.0 s and 0.6 s are defined for the tests where 3 mm·s^{-1} and 5 mm·s^{-1} feed rates are used, respectively.

3.2. Materials

Inconel 718 sheets with a 2 mm thickness are used for LBW tests. This value is similar to the thickness of the sheets used in the aerospace gas turbines. Composition and properties of the material are detailed in Tables 4 and 5, respectively.

Table 4. Inconel 718 composition (wt %) (Haynes® 718 alloy) [36].

Al	B	C	Co	Cr	Cu	Fe	Mn	Mo	Ni
0.55	0.004	0.054	0.28	18.60	0.05	18.60	0.24	3.03	52.40
P	**S**	**Si**	**Ti**	**Nb**	**Ta**	**Bi**	**Pb**	**Ag**	
<0.005	<0.002	0.06	0.98	4.89	<0.05	<0.00003	<0.0005	<0.0002	

Table 5. Properties of Inconel 718 (average thermophysical properties of Inconel 718, Copyright © 2002 Woodhead [37]).

Definition	Unit	Value
Melting range (T_m)	K	1533–1609
Density (ρ)	$Kg{\cdot}m^{-3}$	8190
Specific heat (c)	$J{\cdot}kg^{-1}{\cdot}K^{-1}$	435
Conductivity (k)	$W{\cdot}m^{-1}{\cdot}K^{-1}$	8.9
Latent heat fusion (S_L)	$J{\cdot}kg^{-1}$	210×10^3
Density (ρ_L) (liquid phase)	$Kg{\cdot}m^{-3}$	7400
Specific heat (c_L) (liquid phase)	$J{\cdot}kg^{-1}{\cdot}K^{-1}$	720
Conductivity (k_L) (liquid phase)	$W{\cdot}m^{-1}{\cdot}K^{-1}$	29.6

The developed model is two-dimensional, since most of the laser welding tracks can be considered as longitudinal tracks with constant section. Authors like Casalino asserted, in their research, the suitability of using a two-dimensional model for simulating the LBW process [2]. However, the heat transfer in the experimental situation is tridimensional (including lateral and longitudinal conduction). Therefore, a tridimensional heat transfer is considered in the model. Thus, heat transfer due to conductivity and convection is taken into account in the X, Y, and Z directions, assuming symmetry in the X direction.

3.3. Experimental Setup

Test parts are clamped to avoid distortions caused by thermal expansion or contraction during the melting and solidification process, Figure 7, which could cause misalignment in the weld zone.

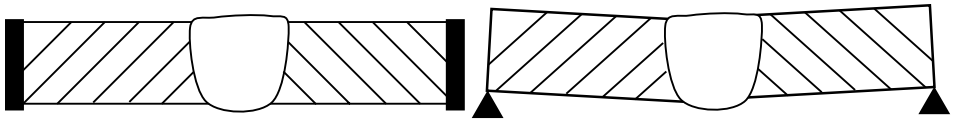

Figure 7. Test part placing examples: properly clamped (**a**) and simply supported (**b**).

The welding process is performed with an argon 2× protective atmosphere (99.995% of argon purity). The argon gas is inserted through four slots situated in four cylindrical tubes: two pointing to the welding upper surface and the two others to the bottom one, which ensures a homogenous supply all along the seam path (see Figure 8). The argon supply is of 24 $l{\cdot}min^{-1}$ (6 $l{\cdot}min^{-1}$ through each 80 mm × 2 mm rectangular slot).

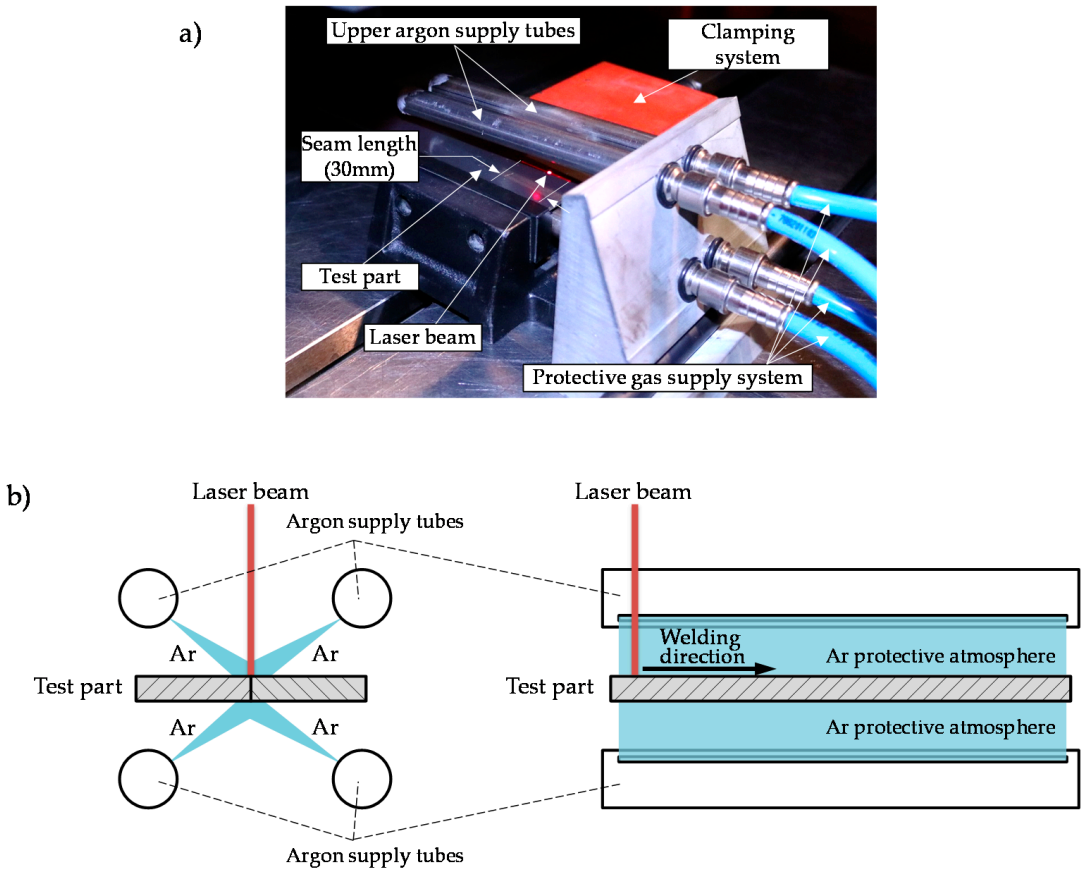

Figure 8. (**a**) Experimental setup for ensuring the protective atmosphere during the laser beam welding (LBW) tests; (**b**) Frontal and lateral schematic views.

4. Results

The developed model calculates the temperature field at different time steps as the laser beam passes over the modeled section. As a consequence of the temperature gradients generated within the molten material, Marangoni forces are generated, and lead to creation of convection currents, see Figure 9. The size of the melt pool is increased as the interaction time increases, and can reach a situation in which the whole thickness of the Inconel 718 sheet is melted (this situation occurs at a t = 0.28 s instant in Test 5, 450 W laser power, and v_f = 3 mm·s^{-1}), and molten material starts to drop due to gravity forces. After the laser beam passes by the modeled cross section and there is no external heat input, the material solidifies, resulting in the final shape of the generated weld bead. This final shape, together with the area melted during the whole process, is compared with the experimental results when validating the model.

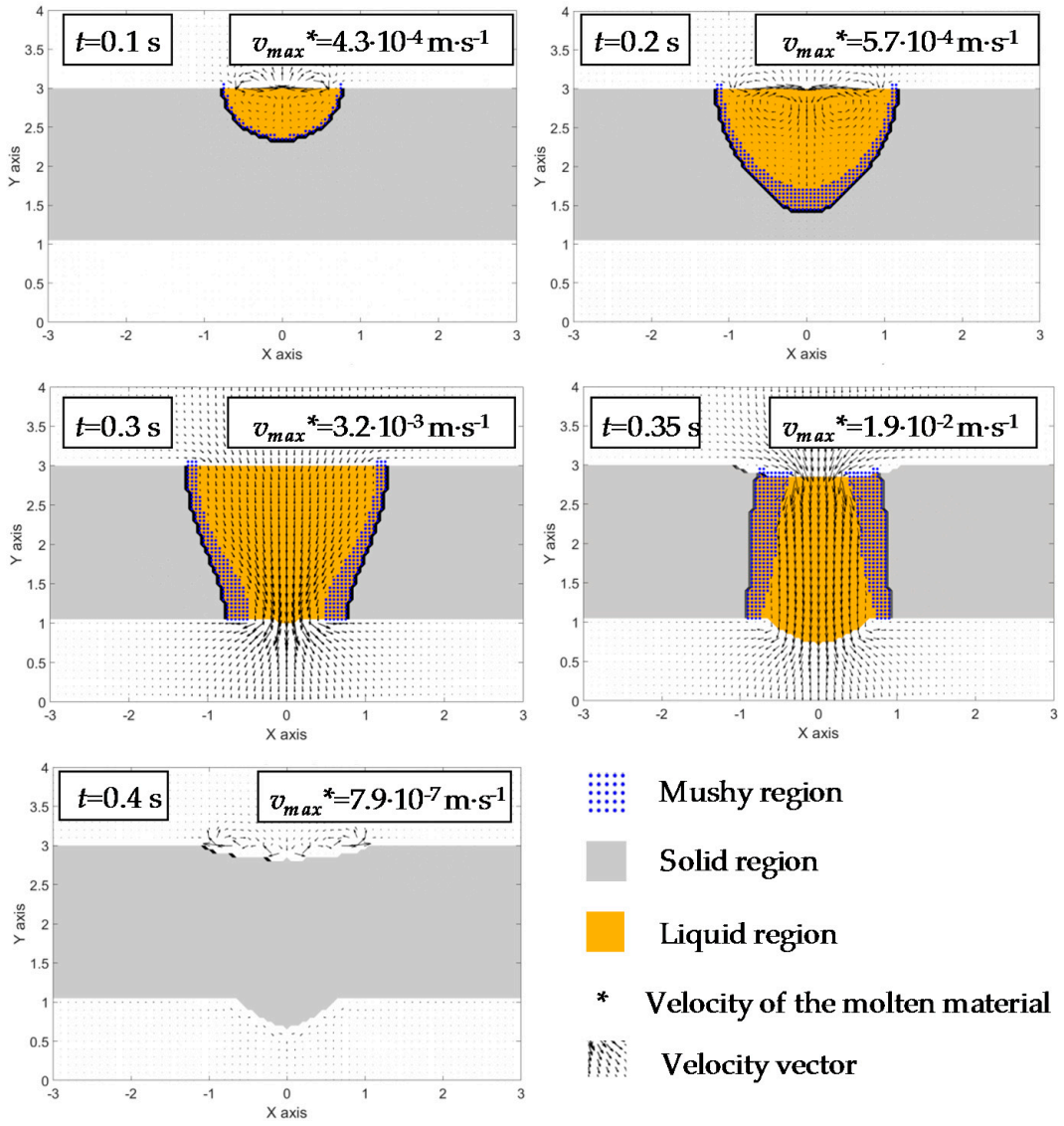

Figure 9. Evolution of the welding section and material velocity for different time steps as the laser beam passes in Test 5.

4.1. Analysis of the Geometry of the Weld Beads

In order to validate the developed model, the weld beads from the different tests are measured, taking into account the following features (see Figure 10): penetration depth (named with the letter D), weld bead width (named with the letter W), and height, both in the crown and the root (named with the letters H and R, respectively). Due to the movement of the molten material during the welding process, the surface tension generates fillets or groovy shapes at the weld crown. The molten material also may stick out at the root when the penetration is complete, forming sagged geometries beyond the lower surface. The established sign criterion is positive (+) for fillets and saggings, and negative (−) for grooves.

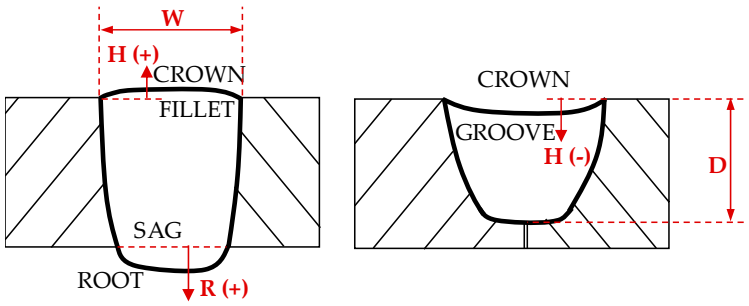

Figure 10. Scheme of the different cross sections of the weld bead (W: crown width; H: crown height; R: root height; D: penetration depth).

The numeric model shows an error below 4% regarding to the weld bead penetration depth and a less than 10% error for the crown width (Table 6). For both the crown and root height prediction, the model shows a maximum error of 0.16 mm (Table 7). Therefore, it is concluded that in those cases in which the weld penetration is complete, the material movement is mainly driven by the gravity forces and the model is capable of predicting this situation with a small error. Nevertheless, for partial weld penetrations, the model has resulted in being incapable of predicting the resulting shape of the bead with the same accuracy, due to the complex fluid dynamic phenomena that occur. In Figure 11, a comparison between the modeled and the measured cross sections is shown for the Tests 1–8.

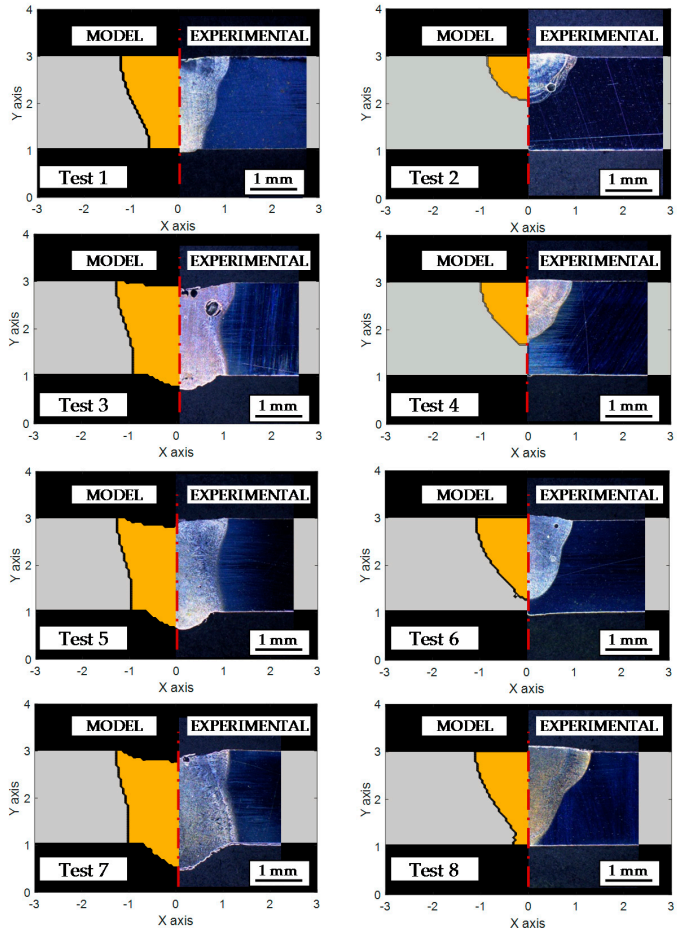

Figure 11. Comparison between the modeled and the analyzed cross sections (tests parameters described in Table 3).

Table 6. Geometrical validation of the model (width and depth).

Test Number	Crown Width (W)			Depth (D)		
	Experimental (mm)	Model (mm)	Error (%)	Experimental (mm)	Model (mm)	Error (%)
1	2.16	2.30	6.38	2.00	2.00	0.00
2	1.98	1.80	9.09	1.09	1.05	3.93
3	2.42	2.50	3.52	2.00	2.00	0.00
4	2.07	2.00	3.19	1.30	1.33	2.47
5	2.56	2.60	1.76	2.00	2.00	0.00
6	2.40	2.20	8.37	1.72	1.75	1.74
7	2.82	2.62	7.13	2.00	2.00	0.00
8	2.61	2.35	9.82	2.00	2.00	0.00

Table 7. Geometrical validation of the model (fillet-groove and sag).

Test Number	Crown Height (H)			Root Height (R)		
	Experimental (mm)	Model (mm)	Error (mm)	Experimental (mm)	Model (mm)	Error (mm)
1	−0.11	0.00	0.11	0.07	0.00	0.07
2	0.09	0.00	0.09	0.00	0.00	0.00
3	−0.16	−0.10	0.06	0.31	0.25	0.06
4	0.04	0.00	0.04	0.00	0.00	0.00
5	−0.20	−0.20	0.00	0.43	0.45	0.02
6	0.16	0.00	0.16	0.00	0.00	0.00
7	−0.16	−0.25	0.09	0.58	0.50	0.08
8	0.10	0.00	0.10	0.07	0.00	0.07

4.2. Microstructure Validation

The internal structure of the material is studied for the Tests 1, 2, 7, and 8, and in each case, as detailed in Figure 12, two different areas are studied for validating the model prediction of the SDAS value. The first one (M1) is located near the boundary between the weld bead and the HAZ, and it is the first area where the material solidifies after its melting, whereas the second one (M2) is placed in the center of the bead.

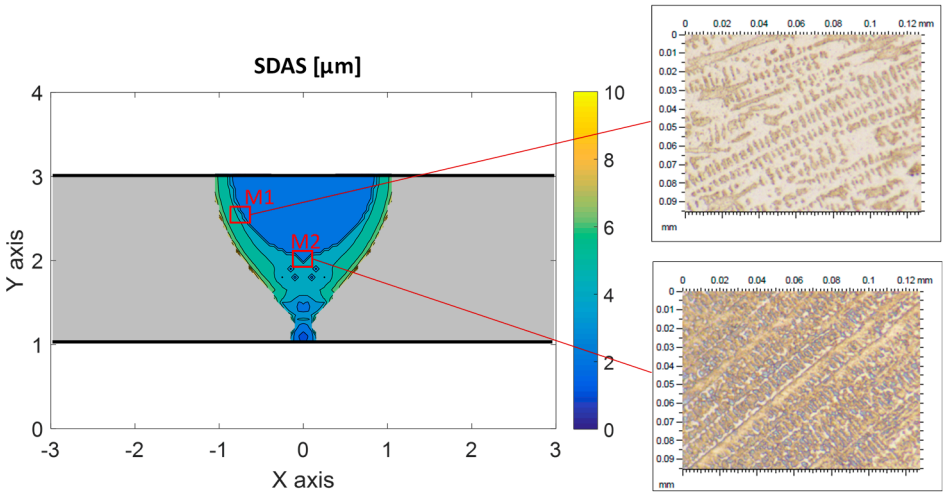

Figure 12. Simulated secondary dendrite arm spacing (SDAS) for cross section and experimental microstructure details in regions M1 and M2 of Test 8 (500 W and 5 mm·s^{-1}).

The analysis of the experimental tests is carried out by a Leica DCM 3D microscopy (Leica Microsystems GmbH, Wetzlar, Germany) with 100× magnification. For each study zone, the SDAS measurements are performed, and the average value is calculated, which is compared with the results given by the numerical model, see Table 8. The maximum error between the predicted SDAS values and the measured ones is below 1.5 microns, which means that there is a good agreement between the

model and the experimental process. Also, since the dendrite formation depends on the cooling rate, which depends on the variation of the thermal field, so, it can be concluded that the model predicts the temperature field accurately during the LBW process.

Table 8. SDAS validation of the model.

Test Number	Area M1			Area M2		
	Model (μm)	Experimental (μm)	Error (μm)	Model (μm)	Experimental (μm)	Error (μm)
1	2.71	3.19	−0.48	2.77	3.70	−0.93
2	2.21	3.05	−0.84	2.04	2.58	−0.54
7	2.31	3.78	−1.47	2.82	4.25	−1.43
8	2.08	3.54	−1.46	1.83	2.63	−0.80

5. Conclusions

In the present work, a numerical model for predicting the weld bead in the LBW process is developed and validated under different process parameters. According to the obtained results, the following conclusions can be drawn:

(1) The developed model represents accurately the weld beads generated under different process parameters. However, the model performance depends on the analyzed bead feature. For instance, an error lower than the 10% is obtained regarding the weld width, whereas a higher accuracy is reached in the weld depth (an error below 4%).

(2) The developed tool is valid for modeling not only the melt pool dynamics, but also the drop of the molten material once the laser beam melts the whole thickness of the Inconel 718 sheets. The error between the model and the experimental results when modeling the crown and root height is below 0.2 and 0.1 mm, respectively. Therefore, it is concluded that the model has a bigger error when dimensioning the weld crown. This is due to the fact that the model is incapable of predicting accurately the height variation of the weld if the penetration is not complete.

(3) After comparing the internal structure measured in the experimental tests and the values given by the model, it is concluded that the model gives the SDAS with an error below 1.5 microns. The two different areas that are analyzed (M1 and M2) show that the SDAS in the test tubes is slightly higher than the value given by the model. Hence, it is concluded that the predicted cooling rate is also somewhat higher than the real one. This can be originated by the symmetry assumption or the two-dimensional solving of the melt pool dynamics, whereas the physical problem is three-dimensional.

Therefore, the proposed model results in being appropriate for modeling the LBW process, and can be used as a predictive tool for simulating weld beads before carrying out real tests. Therefore, it has a direct application in the aerospace industry, and specifically, in Inconel 718 welds. Nevertheless, further work is required in the development of the present model by introducing features such as keyhole formation and temperature-dependent absorptivity, which will improve the accuracy of the model.

Author Contributions: I.H. conceived, designed and performed the experiments; I.H. and J.I.A. developed the numerical model; E.U. and A.L. analyzed the data. A.L. reviewed previous works related with the subject. I.H. and J.I.A. wrote the paper.

Funding: This research received no external funding.

Acknowledgments: Thanks are addressed to H2020-FoF13-2016 PARADDISE project (contract number 723440). Special thanks are addressed to the University of the Basque Country (UPV-EHU) for the funding support received from the contracting call for the training of research staff in UPV-EHU 2015.

Conflicts of Interest: The authors declare no conflict of interest.

References

1. Liu, S.; Mi, G.; Yan, F.; Wang, C.; Jiang, P. Correlation of high power laser welding parameters with real weld geometry and microstructure. *Opt. Laser Technol.* **2017**, *94*, 59–67. [CrossRef]
2. D'Ostuni, S.; Leo, P.; Casalino, G. FEM Simulation of Dissimilar Aluminum Titanium Fiber Laser Welding Using 2D and 3D Gaussian Heat Sources. *Metals* **2017**, *7*, 307. [CrossRef]
3. Li, X.; Wang, L.; Yang, L.; Wang, J.; Li, K. Modeling of temperature field and pool formation during linear laser welding of DP1000 steel. *J. Mater. Process. Technol.* **2014**, *214*, 1844–1851. [CrossRef]
4. Kubiak, M.; Piekarska, W. Comprehensive model of thermal phenomena and phase transformations in laser welding process. *Comput. Struct.* **2016**, *172*, 29–39. [CrossRef]
5. Tsirkas, S.A. Numerical simulation of the laser welding process for the prediction of temperature distribution on welded aluminium aircraft components. *Opt. Laser Technol.* **2018**, *100*, 45–56. [CrossRef]
6. Kazemi, K.; Goldak, J.A. Numerical simulation of laser full penetration welding. *Comput. Mater. Sci.* **2009**, *44*, 841–849. [CrossRef]
7. Venkatesan, K.; Ramanujam, R.; Kuppan, P. Parametric modeling and optimization of laser scanning parameters during laser assisted machining of Inconel 718. *Opt. Laser Technol.* **2016**, *78*, 10–18. [CrossRef]
8. Anderson, M.; Patwa, R.; Shin, Y.C. Laser-assisted machining of Inconel 718 with an economic analysis. *Int. J. Mach. Tools Manuf.* **2006**, *46*, 1879–1891. [CrossRef]
9. Ram, G.D.J.; Reddy, A.V.; Rao, K.P.; Reddy, G.M.; Sundar, J.K.S. Microstructure and tensile properties of Inconel 718 pulsed Nd-YAG laser welds. *J. Mater. Process. Technol.* **2005**, *167*, 73–82.
10. Steen, W.M.; Mazumder, J. *Laser Material Processing*, 4th ed.; Springer: London, UK, 2010.
11. Sun, Z.; Karppi, R. The application of electron beam welding for the joining of dissimilar metals: An overview. *J. Mater. Process. Technol.* **1996**, *59*, 257–267. [CrossRef]
12. Chen, H.; Pinkerton, A.J.; Li, L. Fibre laser welding of dissimilar alloys of Ti-6Al-4V and Inconel 718 for aerospace applications. *Int. J. Adv. Manufact. Technol.* **2011**, *52*, 977–987. [CrossRef]
13. Davis, J.R. *ASM Specialty Handbook: Nickel, Cobalt, and Their Alloys*, 1st ed.; ASM International: Materials Park, OH, USA, 2000; 442p.
14. Dowden, J.M. *The Mathematics of Thermal Modeling: An Introduction to the Theory of Laser Material Processing*, 1st ed.; CRC Press: Boca Raton, FL, USA, 2001.
15. Mazumder, J. Laser welding. In *Laser Materials Processing*, 1st ed.; Bass, M., Ed.; Elsevier: New York, NY, USA, 1983; Volume 3, pp. 120–200.
16. Brown, M.S.; Arnold, C.B. Fundamentals of Laser-Material Interaction and Application to Multiscale Surface Modification. In *Laser Precision Microfabrication*, 1st ed.; Sugioka, K., Meunier, M., Piqué, A., Eds.; Springer: London, UK, 2010.
17. Mills, K.C.; Keene, B.J.; Brooks, R.F.; Shirali, A. Marangoni effects in welding. *Philos. Trans. R. Soc. Math. Phys. Eng. Sci.* **1998**, *356*, 911–926. [CrossRef]
18. Swift-Hook, D.T.; Gick, A.E.F. Penetration welding with lasers. *Weld. J.* **1973**, *52*, 492–499.
19. Klemens, P.G. Heat balance and flow conditions for electron beam and laser welding. *J. Appl. Phys.* **1976**, *47*, 2165–2174. [CrossRef]
20. Goldak, J.; Chakravarti, A.; Bibby, M. A new finite element model for welding heat sources. *Metall. Trans. B* **1984**, *15*, 299–305. [CrossRef]
21. Bonollo, F.; Tiziani, A.; Zambon, A. Model for CO_2 laser welding of stainless steel, titanium, and nickel: parametric study. *Mater. Sci. Technol.* **1993**, *9*, 1137–1144. [CrossRef]
22. Kaplan, A. A model of deep penetration laser welding based on calculation of the keyhole profile. *J. Phys. D Appl. Phys.* **1994**, *27*, 1805–1814. [CrossRef]
23. Ducharme, R.; Williams, K.; Kapadia, P.; Dowden, J.; Steen, B.; Glowacki, M. The laser welding of thin metal sheets: An integrated keyhole and weld pool model with supporting experiments. *J. Phys. D Appl. Phys.* **1994**, *27*, 1619–1627. [CrossRef]
24. Sudnik, W.; Radaj, D.; Breitschwerdt, S.; Erofeew, W. Numerical simulation of weld pool geometry in laser beam welding. *J. Phys. D Appl. Phys.* **2000**, *33*, 662–671. [CrossRef]
25. Tsirkas, S.A.; Papanikos, P.; Kermanidis, Th. Numerical simulation of the laser welding process in butt-joint specimens. *J. Mater. Process. Technol.* **2003**, *134*, 59–69. [CrossRef]

26. Gery, D.; Long, H.; Maropoulos, P. Effects of welding speed, energy input and heat source distribution on temperature variations in butt joint welding. *J. Mater. Process. Technol.* **2005**, *167*, 393–401. [CrossRef]
27. Zhao, H.; Niu, W.; Zhang, B.; Lei, Y.; Kodama, M.; Ishide, T. Modelling of keyhole dynamics and porosity formation considering the adaptive keyhole shape and three-phase coupling during deep-penetration laser welding. *J. Phys. D Appl. Phys.* **2011**, *44*, 485302. [CrossRef]
28. Kubiak, M.; Piekarska, W.; Saternus, Z.; Domanski, T. Numerical prediction of fusion zone and heat affected zone in hybrid Yb: YAG laser + GMAW welding process with experimental verification. *Procedia Eng.* **2016**, *136*, 88–94. [CrossRef]
29. Zhang, L.J.; Zhang, J.X.; Gumenyuk, A.; Rethmeier, M.; Na, S.J. Numerical simulation of full penetration laser welding of thick steel plate with high power high brightness laser. *J. Mater. Process. Technol.* **2014**, *214*, 1710–1720. [CrossRef]
30. Patankar, S.V. *Numerical Heat Transfer and Fluid Flow*, 1st ed.; McGraw-Hill: New York, NY, USA, 1980.
31. Saldi, Z.S.; Kidess, A.; Kenjeres, S.; Zhao, C.; Richardson, I.M.; Kleijin, C.R. Effect of enhanced heat and mass transport and flow reversal during cool down on weld pool shapes in laser spot welding of steel. *Int. J. Heat Mass Transf.* **2013**, *66*, 879–888. [CrossRef]
32. Voller, V.R.; Prakash, C. A fixed grid numerical modelling methodology for convection-diffusion mushy region phase-change problems. *Int. J. Heat Mass Transf.* **1987**, *30*, 1709–1719. [CrossRef]
33. Patel, A.D.; Murty, Y.V. The Effect of Cooling Rate on Microstructural Development in Alloy 718. Superalloys 718, 625, 706 and Various Derivatives. In Proceedings of the International Symposium on Superalloys and Various Derivatives, Pittsburgh, PA, USA, 17–20 June 2001; Loria, E.A., Ed.; TMS (Minerals, Metals, and Materials Society): Warrendale, PA, USA, 2001; pp. 123–132.
34. Antonsson, T.; Fredriksson, H. The effect of cooling rate on the solidification of Inconel 718. *Metall. Mater. Trans. B* **2005**, *36*, 85–96. [CrossRef]
35. Zhang, Y.N.; Cao, X.; Wanjara, P. Microstructure and hardness of fiber laser deposited Inconel 718 using filler wire. *Int. J. Adv. Manufact. Technol.* **2013**, *69*, 2569–2581. [CrossRef]
36. Haynes International. Available online: www.haynesintl.com/alloys/alloy-portfolio_/High-temperature-Alloys/haynes718-alloy/nominal-composition (accessed on 9 July 2018).
37. Mills, K.C. *Recommended Values of Thermophysical Properties for Selected Commercial Alloys*, 1st ed.; Woodhead Publishing: Cambridge, UK, 2002; pp. 181–190.

© 2018 by the authors. Licensee MDPI, Basel, Switzerland. This article is an open access article distributed under the terms and conditions of the Creative Commons Attribution (CC BY) license (http://creativecommons.org/licenses/by/4.0/).